All-optical programmable liquid-crystal photonic circuits

Zala Korenjak[1,2,4], Peter Ropač[1,2,4], Miha Ravnik[1,2], and Matjaž Humar*[1,2,3]

[1] *Condensed Matter Department, J. Stefan Institute, Jamova 39, SI-1000 Ljubljana, Slovenia*
[2] *Faculty of Mathematics and Physics, University of Ljubljana, Jadranska 19, SI-1000, Ljubljana, Slovenia*
[3] *CENN Nanocenter, Jamova 39, SI-1000 Ljubljana, Slovenia*
[4] *These authors contributed equally: Zala Korenjak, Peter Ropač.*
**E-mail: matjaz.humar@ijs.si*

Keywords: liquid crystal photonics, reconfigurable photonic circuits, optical waveguides, topology optimization, all-optical switching

Abstract

Liquid crystals (LCs) have a unique position in optics, combining long-range molecular order with fluidity and strong optical anisotropy. Despite enabling various tunable optical elements, including displays, LCs have not been exploited to realize fully programmable, fabrication-free in-plane photonic circuits. Existing LC waveguides and optical elements typically rely on permanent photoalignment or patterned electrodes, locking the photonic architecture at fabrication. Here, we present a fully reconfigurable planar photonic platform based on optically induced nematic–isotropic phase transitions in LCs. By locally heating a LC cell with a focused infrared beam, we reversibly create isotropic domains that serve as programmable optical potentials with refractive-index contrasts two orders of magnitude greater than in solid-state platforms. Using this approach, we demonstrate a comprehensive library of reconfigurable elements – including waveguides, lenses, beam splitters, diffraction gratings, and all-optical logic gates – which can be combined into functional circuits and redrawn on demand on a ∼100 ms timescale. By integrating topology optimization and inverse design, we achieve optimized functionalities that could serve as a physical photonic breadboard for real-time prototyping of complex architectures. These results establish a fabrication-free platform for adaptive planar optics, with potential in reconfigurable integrated photonics, optical computing, as well as nonlinear and quantum photonic devices.

Liquid crystals (LCs) are soft anisotropic materials whose long-range molecular orientational order enables large and reversible refractive-index modulation via external stimuli such as electric fields, temperature, or light [1], making them a versatile platform for tunable and adaptive optical elements, including lenses, gratings, beam steerers, and spatial light modulators [2, 3].

For planar photonics, in-plane propagation of light within a LC layer makes it possible to construct interconnected optical elements. Various strategies have been developed to engineer spatially varying refractive index, such as photoalignment, which enables precise director control, producing high-quality LC waveguides, lenses, and gratings [4–8], while patterned electrodes provide electrically tunable beam steering, waveguiding, and diffraction [9–12]. An alternative soft-matter approach harnesses intrinsic optical nonlinearities in nematic LCs: reorientational nonlinearity forms nematicons – self-localized beams that enable dynamic steering and switching [13–15], while material chirality can further enhance the periodic self-focusing

and guiding of light in such birefringent media [16]. Beyond self-guided beams, recent work has shown that engineered director landscapes and disorder in nematic LCs can be used to control light through topological effects and complex refractive-index environments, enabling phenomena such as topological beam steering [17, 18] and branched flow of light [19, 20]. While these methods showcase the richness of LC soft matter as an optical medium, they typically rely on predefined, static director patterns, limiting real-time reconfigurability and arbitrary reprogramming.

Reconfigurable integrated photonics has developed across several material platforms, including programmable silicon photonic circuits [21], phase-change photonics [22], MEMS-based photonics [23], and optofluidic infiltration of pre-fabricated photonic crystals [24, 25]. These optofluidic approaches, in particular, tuned the optical response of a fixed, lithographically defined architecture rather than creating the circuit itself. Semiconductor platforms have recently enabled wave-based computing and neuromorphic applications [26, 27]; however, the achievable refractive-index modulation is relatively small ($\Delta n \sim 10^{-4} - 10^{-3}$) and typically requires complex fabrication and control architectures. In contrast, LCs provide refractive-index tunability that is approximately two orders of magnitude larger. This large index contrast (up to $\Delta n \approx 0.12$) enables not only gradual phase modulation and wavefront shaping, but also total internal reflection, spatial light confinement and waveguiding with bend radii of $\sim$100 µm, and beam steering over up to 90° (SI-Video 1), making them a natural candidate for programmable photonic circuits.

In parallel, inverse design via topology optimization has become a vital tool for developing high-performance photonic structures beyond intuitive rules [28]. In solid-state photonics, it has enabled diverse components, including compact photonic crystals [29], slow-light devices [30], waveguides [31, 32], (de)multiplexers [33, 34], metasurfaces [35, 36], non-reciprocal devices [37], and photonic logic [38]. Modern implementations ensure fabricability through rigorous constraints, projections, and filtering [39, 40]. However, while mature in solid-state systems, topology optimization is still nascent in soft-matter and LC photonics, where anisotropy, phase transitions, and reconfigurability introduce unique complexities and design opportunities. We address a tractable sub-problem: for E_z-polarized light with an in-plane director the design reduces to a single scalar dielectric component, letting us apply established density-based methods and handle the majority of soft-matter–specific physics in the surrounding pipeline.

Here, we introduce a fabrication-free photonic platform that leverages optically induced phase transitions to create reconfigurable refractive-index landscapes. We first demonstrate a comprehensive library of individually reconfigurable elements — waveguides, lenses, beam splitters, diffraction gratings, and all-optical logic gates. We then show these can be combined into functional photonic circuits within a single unmodified LC cell.

Finally, we introduce a soft-matter-specific inverse-design pipeline that transcends intuitive design while mapping the design onto a realizable layout of laser-written isotropic domains, establishing this platform not merely as a collection of optical components but as a fully programmable photonic breadboard.

Results

Control of laser beam with isotropic droplets in nematic liquid crystal

The photonic platform presented here operates on a straightforward principle: a focused infrared beam locally drives the LC from the nematic to the isotropic phase, creating an optically distinct domain whose size, shape, and position can be controlled in real time by modulating the laser beam. The experimental setup (Fig. 1a) consists of a LC cell with a gap of 4 µm or 9 µm, filled with 5CB LC, as shown in Fig. 1b. Polarized laser light is focused into the gap from the side

using an aspheric lens, so that in most cases the director of the aligned LC layer is perpendicular to the coupled laser beam. To manipulate in-plane beam propagation, we induce refractive index variations by locally heating the LC from the nematic to the isotropic phase. This is achieved

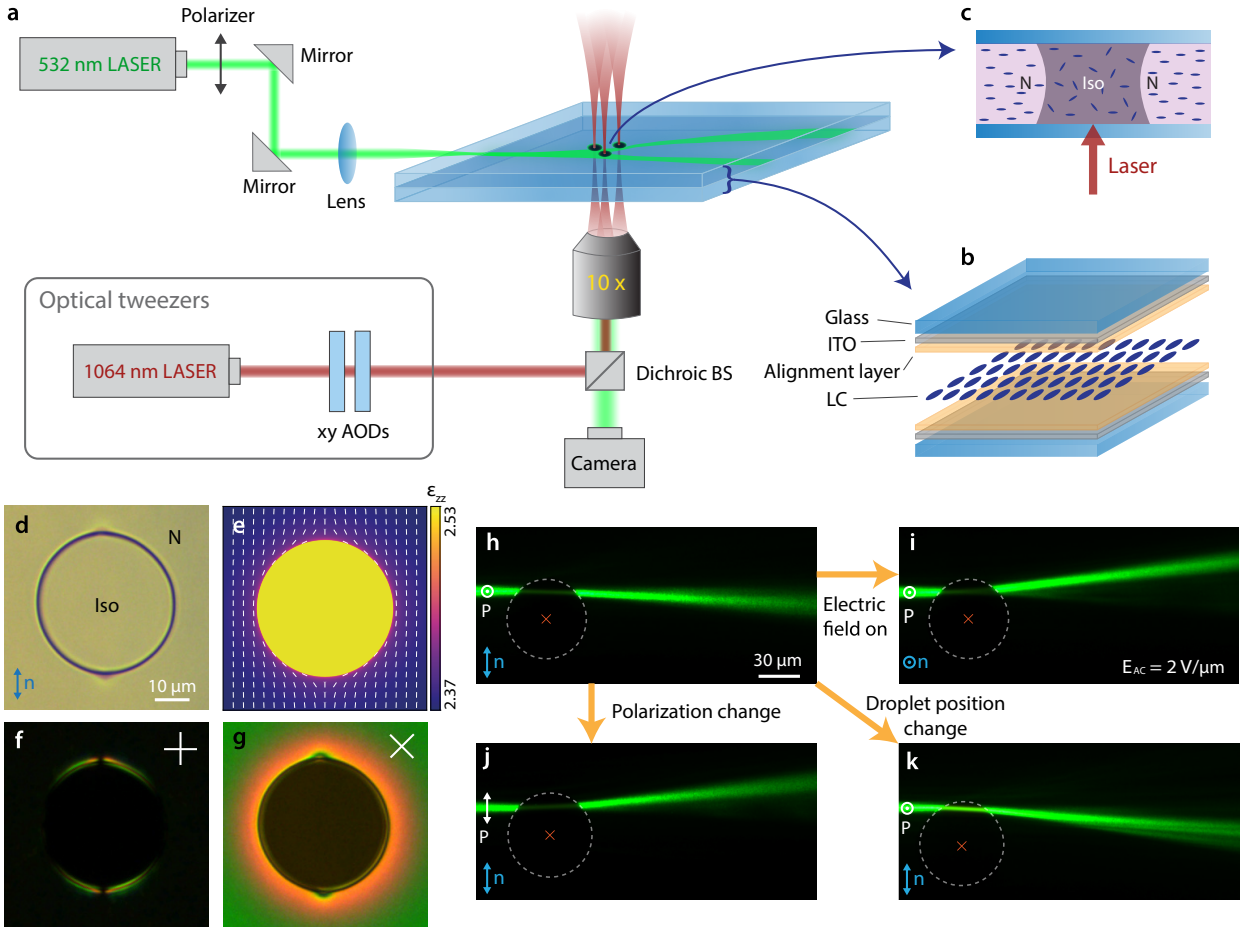

Figure 1: Isotropic laser-induced droplet in nematic liquid crystal for in-plane beam control. (a) Schematic of the experimental setup for in-plane beam control. The laser beam is focused into the LC cell from the side. An optical tweezers with an infrared continuous-wave laser and two acousto-optic deflectors (AODs) are used to locally heat the LC cell. An image of the in-plane beam propagation is captured with a camera. (b) Schematic of the LC cell structure. (c) Formation of an optically induced isotropic droplet within the nematic background at the control beam focus. (d) Image of an isotropic droplet in bright field. (e) Simulation of the director configuration in the nematic phase around the isotropic droplet (white lines) and dielectric permittivity ε_{zz} for light polarized perpendicular to the LC layer. Dielectric permittivity outside the isotropic droplet gradually decreases due to a temperature drop. (f) The same droplet with added crossed polarizer and analyzer parallel to the director orientation and (g) at an angle of 45° with respect to the director. The director orientation in the nematic phase is marked with a blue arrow, and the direction of the polarizers is indicated with a white cross. (h) Image of the scattered light from the in-plane laser beam with polarization perpendicular to the LC cell. The beam strikes the isotropic droplet, marked with the white dashed line, at the upper half of the droplet and is deflected toward the center of the droplet. The position of the control beam focus is marked with a red cross. (i) The same beam position and isotropic droplet as in (h), but with applied electric field, which reorients the director in the direction perpendicular to the LC cell. This causes the beam to deflect away from the center of the droplet. (j) The same effect can be achieved without an electric field by changing the polarization of the in-plane beam to be parallel with the director. (k) When the beam hits the droplet closer to the edge, the reflected angle compared to (h) changes.

using an infrared (1064 nm) continuous wave laser in a tweezers configuration, which is focused into the LC cell from below. Glass plates in the LC cell are coated with a thin layer of indium tin oxide (ITO), which strongly absorbs infrared light. At the IR beam focus, a small isotropic droplet appears (Fig. 1c). To create patterns of isotropic regions, the control beam focus is rapidly switched between multiple defined positions using acousto-optic deflectors (AODs) – the same-time-sharing principle used in multi-trap optical tweezers – effectively maintaining up to hundreds of independent isotropic domains simultaneously. With a control IR beam with an average power ranging from 8 mW and 100 mW, isotropic droplets with diameters ranging from 5 µm and 150 µm can be created (Fig. 1d). The droplet boundary corresponds to the isotherm at which the LC reaches the nematic–isotropic transition temperature; because heat conduction is essentially linear, the quasi-steady-state temperature rise scales with the absorbed power, so increasing the control-beam power raises the temperature profile and moves this isotherm outward, monotonically increasing the domain size (SI-Fig. 1a). When the beam is time-shared over many positions, the AOD switching rate (100 kHz) is far faster than the thermal response of the LC (tens of milliseconds), so each location experiences an effectively constant, time-averaged heating rather than the instantaneous on/off modulation. The size of each domain is therefore set by the time-averaged power it receives, and meaningful domain sizes are maintained as long as this per-position average power stays within the range above; distributing the beam over more positions lowers the average power per position at fixed total power, which is compensated by increasing the total power or the dwell time allocated to each position. Two defects are visible at the edge of the droplet along the rubbing direction, representing a boojum configuration (Fig. 1e). In the vicinity of the isotropic droplet surface, the nematic director tilts toward the droplet interface due to planar anchoring at the nematic–isotropic boundary (Fig. 1f). Due to heat diffusion, the temperature of the LC around the droplet gradually drops to room temperature, causing a continuous change in LC birefringence (Fig. 1g).

When the in-plane beam impinges on an isotropic droplet, it is deflected due to the difference in refractive indices between the two phases. When the polarization of the in-plane beam is perpendicular to the LC layer the beam experiences the ordinary refractive index, which is lower than the refractive index of the isotropic phase ($\Delta n_{\mathrm{o}} = n_{\mathrm{iso}} - n_{\mathrm{o}} \approx 0.05$). This causes the beam to refract toward the droplet center by a few degrees (Fig. 1h). The beam path is especially visible in the nematic phase due to Rayleigh scattering [41]. There are three distinct ways to manipulate the light: by applying an electric field, changing the polarization of the in-plane beam, or by moving the isotropic droplet (Fig. 1i-k). The refractive-index contrast between the isotropic droplet and the nematic phase can be inverted ($\Delta n_{\mathrm{e}} = n_{\mathrm{e}} - n_{\mathrm{iso}} \approx 0.12$) — and the beam deflected away from the droplet — either by applying an electric field to reorient the director homeotropically (Fig. 1i), or by switching the beam polarization to be parallel to the director (Fig. 1j). While uniform ITO electrodes are used here for global switching, they can readily be replaced with patterned electrodes, thereby adding a secondary layer of spatially resolved electrical control to the optically programmed circuits. If the size or position of the droplet is changed, the angle of the refracted beam also changes (Fig. 1k).

The isotropic droplets can be smoothly translated, dynamically changed in size and shape over time by adjusting the power of the control beam and rapidly switched on and off. The formation of an isotropic droplet after activation of the control beam typically occurs within 100 ms (see SI-Fig. 1b), while the switching-off process is even faster, with characteristic times in the range of $30 - 50$ ms. The switching dynamics depend on the droplet size and the temperature of the surrounding nematic phase. Since reconfiguration is limited by droplet formation ($\sim$100 ms) and relaxation (30-50 ms) rather than by the AOD beam repositioning (100 kHz), a complete circuit can be rewritten within $\sim$100 ms. These times are comparable to conventional nematic LC modulators (a few to tens of milliseconds) and optofluidic systems, but slower than thermo-optic (microseconds), MEMS (microseconds to milliseconds), and phase-

change (nanoseconds) platforms – a trade-off offset by the two orders of magnitude larger refractive-index contrast and the fully fabrication-free, arbitrarily reprogrammable geometry. Scaling to larger and denser circuits is ultimately constrained by thermal diffusion, which sets a minimum spacing between independently addressable elements to avoid thermal cross-talk; in practice we already maintain up to hundreds of domains simultaneously, with periodicities down to 25 µm in the diffraction gratings. The overall circuit extent is currently also limited by the microscope field of view (of the order of 1 mm for the 10× objective used here), a constraint that would be lifted by electrical rather than optical addressing (see Discussion). These tens-of-millisecond switching times are a genuine limitation for high-speed photonic applications, but they are on par with the nematic LC devices already in widespread use and are well suited to reconfiguration and real-time prototyping. The all-optical nature of our platform inherently supports ultrafast phenomena, possibly allowing modulation on a 500 fs timescale via the optical Kerr effect [42]. While this ultrafast regime does not induce isotropic domains and yields a considerably smaller refractive-index modulation than our thermal approach, it could, in the future, provide a high-speed modulation that is completely inaccessible to conventional electric-field LC switching.

Beam steering, waveguides and lenses

To steer the in-plane beam, we use multiple isotropic droplets along the beam path (Fig. 2a, left). Using an angled array of isotropic droplets, we can achieve a parallel shift of the beam. If the control beam focal positions are close together, individual isotropic droplets melt together, forming different, distinct, and designable shapes. In the case shown in Fig. 2a (right), five focal positions form long elliptical lines. By using in-plane polarization of the beam, it can be steered upward and downward by total reflection from the angled lines located on both sides of the beam. The input beam is Gaussian and, for such beam-steering elements, retains an approximately Gaussian profile along propagation, whereas after multiple cascaded elements the output mode can become more complex.

In-plane laser light can also be guided within the isotropic phase (SI-Fig. 2a, SI-Video1). To test a curved waveguide, we created a large semicircular isotropic region on the edge of the LC layer (Fig. 2b). The laser light was guided along the isotropic-nematic boundary through multiple total internal reflections. In this case, instead of scattered laser light, fluorescent light was observed. Fig. 2b (right) shows that the simulated intensity in the curved waveguide matches with the measured fluorescent light in Fig. 2b (left). Waveguide losses were determined from the fluorescence intensity along the curved path, starting after the first leakage point (Fig. 2b), with the intensity profile shown in Fig. 2c. The intensity decays exponentially with distance, with small oscillations caused by reflections at the isotropic-nematic boundary. Total attenuation ($A = A_{\text{waveguide}} + A_{\text{losses}}$) includes losses due to curvature, absorption in the LC and the added dye, and scattering. Curvature-induced losses decrease exponentially with radius (Fig. 2d), and the asymptotic value attributed to absorption and scattering loss A_{losses} is $(1 \pm 0.4) \times 10^{-3}\,\mu\text{m}^{-1}$ (≈4 dB/mm). This enables propagation over hundreds of micrometers, sufficient to support multi-component photonic circuits. The large refractive index contrast effectively confines light even in bends with radii of order 100 µm, enabling compact circuit layouts that offset propagation losses by minimizing the required device footprint.

Small circular isotropic droplets can also be used as lenses (Fig. 2e). Varying the control beam power in real time from 6 mW to 18 mW smoothly modulated the droplet diameter from 3 µm to 37 µm, shifting the beam focus. The focal length, measured as the distance from the droplet where the intensity is highest, is linearly proportional to the droplet diameter (Fig. 2f). The measurements matched the calculated dependence of the focal length of a circular lens on its radius in the paraxial approximation. By using additional positions of the control

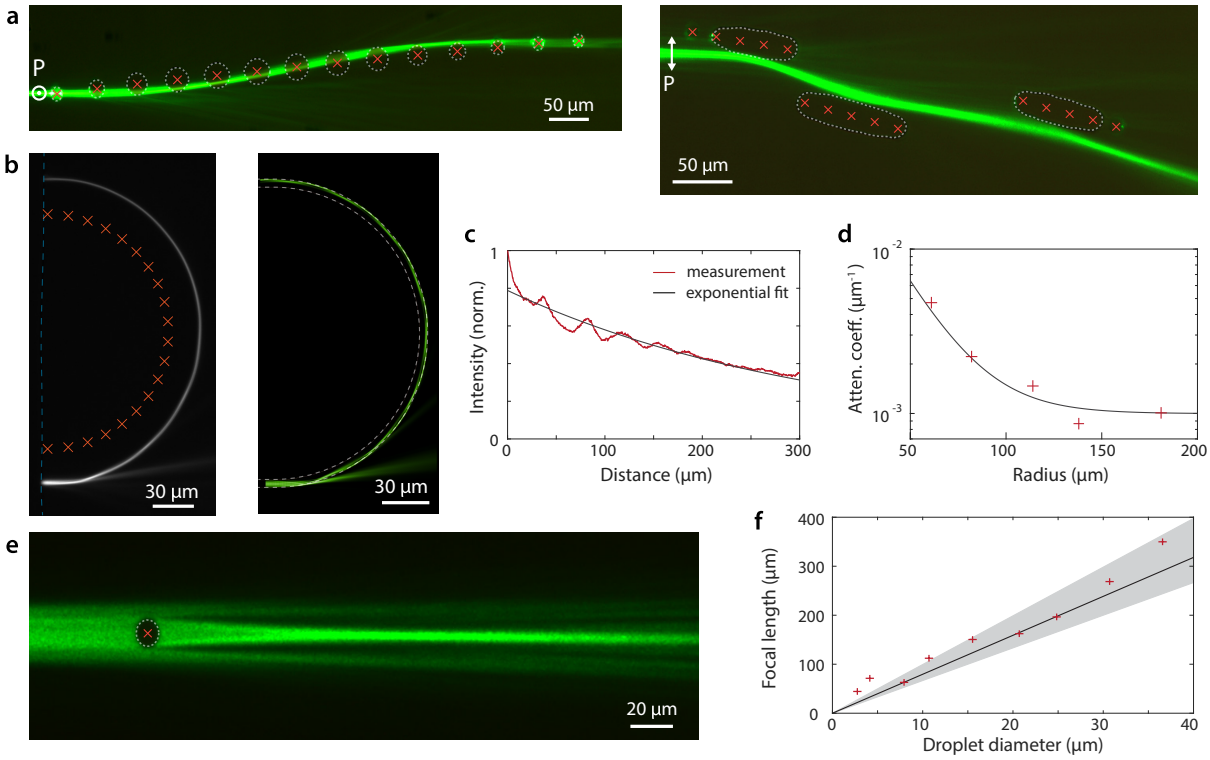

Figure 2: Beam steering, curved waveguides and lenses. (a) Image of a parallel beam shift with an angled array of 14 isotropic droplets (left), and beam steering by total reflections from isotropic lines created with five focal positions of the control beam (right); in the latter case, the polarization of the beam is in-plane, parallel to the director. (b) Monochrome image of fluorescent light showing the path of the laser light guided along the edge of the semicircular isotropic droplet with a radius of 114 µm (left); the isotropic region is positioned at the edge of the LC layer, so the laser beam is focused directly into the isotropic phase, and the edge between the LC layer and the glue closing the LC cell gap is marked with a blue dashed line. Simulated light guided on the edge of the curved waveguide (right). (c) Intensity profile of fluorescent light along the curved edge in (b), shown by the red line. The black line is the exponential decay fit function. (d) Attenuation of light in the curved waveguide for different radii of curvature (red crosses) and exponential fit ($A = a\,e^{-CR} + A_{\text{losses}}$) (black line). (e) A small isotropic droplet with a diameter of 11 µm focusing light acts as a lens. (f) Focal length as a function of droplet diameter. Red crosses represent the measurements; the black line shows the model function, with the gray area indicating the range of possible refractive indices used in the model.

beam, lenses with different shapes can be created (SI-Fig. 2b-d), and their focal length can be adjusted in real time (SI-Video 2), opening the possibility of aspheric or otherwise customized lens geometries. Furthermore, by applying an electric field, the same isotropic structure can be switched between convex and concave behavior (SI-Fig. 2c-d), providing an additional degree of tunability.

Beam splitters

In addition to waveguides and lenses, isotropic droplets can be used to easily design beam splitters. A pair of droplets placed side by side, perpendicular to the incoming beam, forms a wavefront-splitting beam splitter (Fig. 3a), with the splitting ratio continuously tunable by shifting the pair perpendicular to the incident beam (SI-Video 3). When centered (Fig. 3a, left), the ratio is ≈ 0.5; shifting the pair off-center increases the intensity in the beam closer to the droplet nearest the input beam (Fig. 3a, right). Figure 3b shows a linear dependence of the splitting ratio on droplet position. In addition, the angles between the exiting beams can

be adjusted by rotating the pair of droplets with respect to the direction of the incoming beam (SI-Fig. 3c-e). By adjusting the distance between the droplets and adding additional droplets, it is possible to split the beam into three or even more exiting beams (SI-Fig. 3a-b), each of the beams with tunable angle and intensity. Because nematic LCs are intrinsically birefringent, the platform naturally supports polarization-sensitive elements: even a single isotropic droplet (Figs. 1h,j) can split unpolarized input light into two orthogonally polarized beams (see SI-Fig. 9 for a more complex example).

The functionality of the isotropic structure depends on its shape: micrometer-scale shifts of a control beam, sub-milliwatt power changes, or adding a focal position can alter its effect – dynamically and in real time. A clear example is switching between a beam splitter and a lens (Fig. 3c). With two isotropic droplets, the structure acts as a beam splitter, while adding a third control beam focus between them expands the isotropic region into a focusing lens that reshapes the incident wavefronts and negates the beam-splitting effect, as shown also by Finite Difference Time Domain (FDTD) simulations (Fig. 3c). The resulting angular output profiles (Fig. 3d) clearly distinguish the two modes, demonstrating optical switching via the third beam focal position.

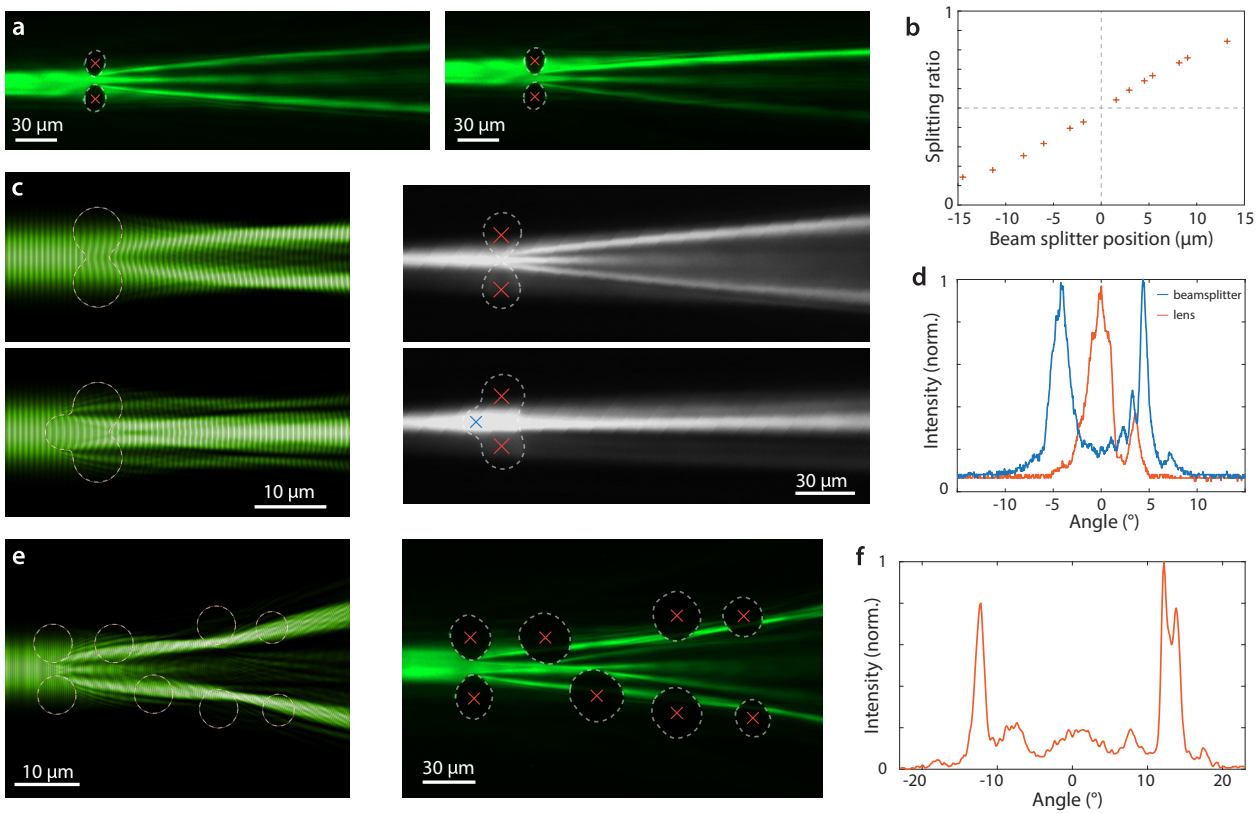

Figure 3: Beam splitters and topological optimization. (a) Image of a beam splitter made with two isotropic droplets positioned symmetrically to the incoming beam, with a splitting ratio of approximately 0.5 (left), and the same beam splitter shifted with respect to the beam center, giving a splitting ratio of 0.3 (right). (b) Plot of the splitting ratios with respect to the position of the isotropic droplet pair center. (c) Simulations (left column) and fluorescence images (right column) of the beam splitter (upper) and the lens (lower); the fluorescence beam splitter is created with two control beam foci with the average power of 20 mW, and the lens with an additional control beam focus (average power 4 mW) between the droplet pair. (d) Intensity profile of the angular distribution of the exiting beam, comparing the beam splitter isotropic structure (blue line) and the lens isotropic structure (orange line) from (c). (e) Simulation (left) and experimental realization (right) of the topology optimized beam splitter. (f) Intensity profile of the two exiting beams from (e).

While the structure with only two isotropic droplets can work as a beam splitter, the two beams are split by only roughly 10°. To design a beam splitter with greater beam separation, we used a custom inverse design approach based on topology optimization (see Methods), where the output of the algorithm is the positions of the control beams and ideal isotropic disk sizes. The developed inverse design framework accounts for the anisotropic director field, temperature-dependent refractive indices, and the minimum feature sizes imposed by the physics of isotropic droplet formation. Fig. 3e shows the steady-state intensity distribution for one of the inversely designed structures (see SI-Fig4 for more examples). The experimental realization of the optimized structure and its intensity profile are shown in Fig. 3e,f. The intensity distribution in Fig. 3e shows a good match between the experimentally realized structure and simulations and validates the inverse design approach. The intensity profile shows that the beams are split at the designed angle, which was set to be much greater compared to the beam splitters shown previously. Notice that the optimized structure is not symmetric, but achieves a well-symmetric split in the output beam intensity. This successful implementation demonstrates that our inverse design framework achieves the prescribed splitting angle of $\sim$25°, much larger than that of the intuitive two-droplet design.

Diffraction gratings, optical switches and complex optical circuits

The versatility of our platform extends to diffractive optical elements, enabling wavelength-sensitive functionality beyond simple beam manipulation. Diffraction gratings were created using an array of control beams, producing a one-dimensional periodic variation in refractive index. Figure 4a shows a diffraction grating with 25 µm periodicity. When a broad, coherent laser beam passes through this diffraction grating, a diffraction pattern is clearly visible. The intensity profile measured 1 mm from the grating (Fig. 4b, green line) shows pronounced modulation. We simulate the diffraction pattern at the same distance from the structure using the FDTD solver and its integrated near-to-far field propagator. The simulated diffraction pattern (Fig. 4b, black line) is in good agreement with the experimental results. Furthermore, we simulate the diffraction patterns for different wavelengths (SI-Fig. 5), which opens immediate prospects for reconfigurable wavelength-selective devices, including miniaturized spectrometers, wavelength multiplexers and demultiplexers, and tunable optical filters.

Beyond passive optical elements, our platform also enables active all-optical devices in which the in-plane signal beams themselves participate in shaping the photonic circuit. This is achieved by exploiting the absorption of the in-plane beams in the ITO layer, which generates additional local heating that modifies the isotropic LC structures created by the control beam. Logic gates were realized by forming isotropic structures with the control beam and reshaping them through different combinations of red (674 nm) and blue (450 nm) in-plane beams. The two input channels co-propagate and spatially overlap – they are combined with a dichroic mirror and focused through the same lens – differing only in wavelength; the type of logic gate is therefore determined solely by the pre-written isotropic structure, so that with identical input beams all gates can be realized simply by reconfiguring the melted zones with the control beam. An experimental example of an XOR logic gate is shown in Figures 4c–e. An isotropic structure acting as a beam splitter is formed using the control beam. With only the blue beam (Fig. 4c) or only the red beam (Fig. 4d) on, the structure splits the beam so that one beam reaches the output port. When both beams are on (Fig. 4e), the additional heating reshapes the structure so that both beams pass through without redirection and no light reaches the output. Figure 4f shows the exiting intensity for all three cases, with a peak in the output region (yellow shaded) whenever exactly one beam is on, and its suppression when both are on, as summarized in the truth table shown in Fig. 4f. In addition to the XOR logic gate, we showed examples of AND and INH (inhibit) logic gates (SI-Fig. 6), which together form a functionally complete set.

An AND operation does not, in principle, require a nonlinear interaction between the input beams, as it can be obtained by linear summation of their powers followed by thresholding, a decision nonlinearity that any digital gate ultimately requires. In our platform, however, all gates – including AND – operate through the same nonlinear thermal pathway, in which the combined absorption of the co-propagating beams in the ITO reshapes the isotropic structure. The XOR gate relies critically on this nonlinearity, since its output must be suppressed when

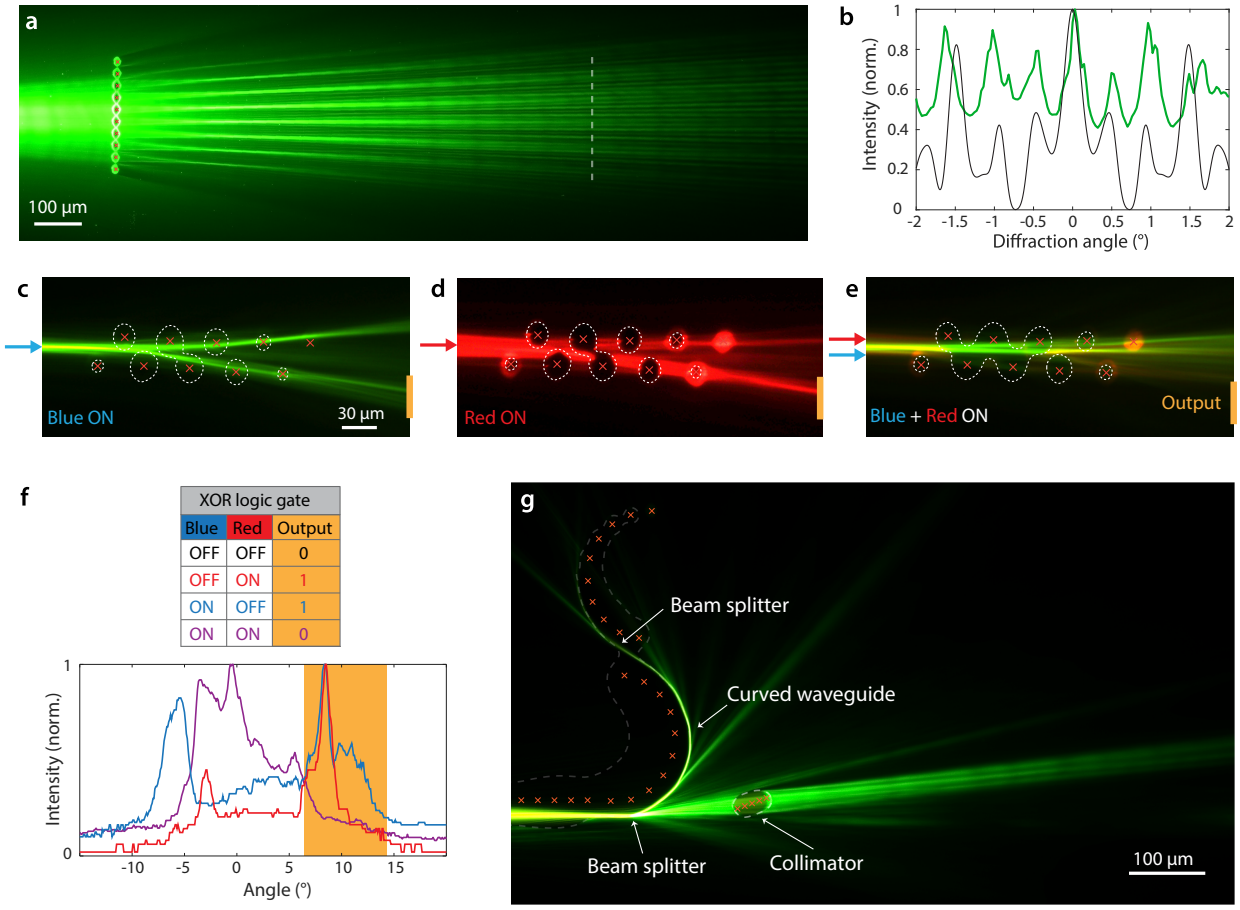

Figure 4: Diffraction gratings, optical switches, and a combination of optical elements. (a) Image of a diffraction grating with a periodicity of isotropic droplets of 25 µm. The diffraction pattern is visible at large distances from the diffraction grating. (b) Intensity profile of the diffraction pattern at 1 mm from the grating. The green line shows the measured intensity along the white dashed line in (a). The black line shows the simulated intensity profile. (c) Experimental example of an XOR logic gate. Only the blue 450 nm laser beam is turned on, and the image is taken in fluorescent light. The isotropic structure acts as a beam splitter, and one of the beams reaches the output port, marked with a yellow line. (d) The same example with the red (674 nm) laser turned on; the structure again splits the beam so that one beam reaches the output port. (e) Both red and blue lasers are turned on. Due to the additional heating when both beams are absorbed in the ITO layer, the beam-splitter structure is reshaped so that both beams pass through without redirection and no light reaches the output port. (f) Intensity distribution at the right end of images: (c) blue line, (d) red line, and (e) purple line. When only one laser is on, a sharp peak appears in the output region (yellow area); when both are on, the peak vanishes. The truth table for the XOR logic gate is shown above the intensity plot in (f). (g) Image of a combination of optical elements: two beam splitters, a curved waveguide, and a collimator. The in-plane beam is focused into the isotropic phase, where part of it is guided along the edge of the curved waveguide and split using a C-shaped isotropic structure, while the other part is collimated by a lens.

both beams are present, which cannot be achieved by linear power summation. In all previous cases (waveguides, beam splitters, lenses, etc.), the in-plane beam power was approximately ten times lower, making it insufficient to induce any structural modifications on its own.

The final demonstration of a photonic platform is not individual elements in isolation, but their integration into a functional circuit. Figure 4g shows three distinct optical elements — a beam splitter, a curved waveguide, and a collimator — operating simultaneously within a single LC cell, with light routed between them as in a planar optical circuit. Crucially, each element can be independently retuned or erased while the others remain active, demonstrating the true reprogrammability that distinguishes this platform from all existing LC photonic approaches. For example, by adjusting the positions of the control beam, we can tune the path and proportion of forward-propagating light, which is then collimated with an elliptical droplet.

As a further illustration of the platform's potential, preliminary results suggesting a Rayleigh interferometer [43] are presented in the Supplementary Information (SI-Fig. 7), where a beam splitter divides the incoming light and an isotropic structure recombines it. Changing the droplet size in one arm alters the interference pattern at recombination.

The same platform that enables deterministic photonic circuits also provides a natural testbed for studying light propagation in smooth disordered potentials — a regime inaccessible to rigid solid-state platforms. By randomly placing isotropic droplets, we realize a correlated random refractive-index landscape [20] and observe branched flow of light (SI-Fig. 8), connecting our platform to fundamental wave transport physics [19, 44, 45].

Discussion

Here, we present a fully programmable planar photonic platform based on optically induced nematic–isotropic phase transitions in LCs. By eliminating the need for permanent microfabrication, photoalignment, or fixed electrode geometries, our approach enables reversible, real-time control of refractive-index landscapes for in-plane light propagation. This is a fundamental departure from earlier reconfigurable photonic-crystal platforms, where microfluidic infiltration tunes the response of a pre-fabricated structure [24, 25]: here the photonic elements themselves are written and erased on demand within an unstructured cell, with no underlying fabricated architecture. By dynamically shaping isotropic regions within a nematic background, we demonstrate a wide range of fundamental planar optical elements within a single LC cell, with no precedent in LC photonics.

Building on our demonstration of multi-component integration, this method could enable compact optical devices such as miniaturized spectrometers and support reconfigurable routing networks, optical computing, and optical information processing [26]. Optical computing is pursued across a broad range of length scales. The minimum feature size of our platform, set by thermal diffusion and the control-beam focus, is a few micrometres, so it cannot reach the sub-micrometre scale of dense integrated single-mode photonic circuits [21]; it is, however, well suited to in-plane, multimode wave-propagation approaches to optical computing [26] that operate at larger length scales, and finer features could be reached with a shorter control-beam wavelength, higher-numerical-aperture focusing, and thinner cells. Additionally, optical elements that can be implemented and rewritten on demand could create a lithography-free photonic breadboard for rapid prototyping of integrated in-plane circuits. Such a platform may be especially powerful when combined with real-time, in-situ inverse design. Coupling the optimization loop directly to the physical platform — measuring the optical response and updating the control-beam pattern in situ — could enable closed-loop, self-adaptive photonic circuits that correct for aberrations and drift in real time.

Important directions for future work include the realization of active photonic elements capable of optical gain and lasing, as well as fully electrically driven architectures. LCs readily

accommodate fluorescent dyes, enabling optical gain within the same medium used for beam control, which opens the possibility of reconfigurable microlasers [46–48]. Further, instead of optical addressing, a fully electrically driven planar, pixelated device could function as an integrated in-plane spatial light modulator. Such an architecture would modulate light propagating directly within the device plane, thereby reducing device size and removing the optical field-of-view limit on circuit scale, in principle allowing arbitrarily large circuits. The specific optical method used to generate the heating pattern is also not fundamental to the approach: here we used AOD-based optical tweezers that were readily available and provide precise, high-power, rapidly reconfigurable multi-spot addressing, but the same patterns could equally be projected with an LCOS spatial light modulator, building on early concepts of optically defined interconnections in waveguides [49].

Furthermore, operating the control beam at lower power can precisely tune the temperature within the nematic phase, enabling the writing of smooth, continuous refractive-index gradients. While yielding slightly lower maximum contrast, this regime is ideal for gradient-index (GRIN) optics, low-loss adiabatic waveguides, and analog phase shifters.

Beyond the specific devices demonstrated, the soft-matter inverse design framework introduced here represents a methodological advance for LC photonics. Unlike solid-state topology optimization, which operates on fixed dielectric profiles, our approach must account for continuously varying, temperature-dependent refractive indices whose profile is governed by heat diffusion and set by the proximity to the isotropic zones. The three-stage inverse design pipeline — topology optimization, temperature-profile matching, and photonics shape optimization — provides a general framework that should extend to other LC optical design problems.

Finally, this platform could serve as a soft-matter counterpart to recent advances in semiconductor-based programmable nonlinear photonic circuits [27]. In particular, emerging ferroelectric nematic LCs, which exhibit strong spontaneous polarization and a second-order nonlinearity ($\chi^{(2)}$) several orders of magnitude higher than reported in [27], could enable not only second-harmonic generation (SHG) but also spontaneous parametric down-conversion (SPDC). This capability would enable tunable nonclassical light sources, including entangled photon pairs [50, 51], paving the way for fully liquid-crystal-based, adaptive quantum photonic circuits.

Methods

Materials and preparation of liquid crystal cells

The material used in experiments was 4-Cyano-4'-pentylbiphenyl (5CB) liquid crystal with the nematic-isotropic transition temperature of 33.5 °C [52]. In some samples, the fluorescent dye Pyrromethene 597 (Exciton) was added to the LC at a concentration of 2.7×10^{-4} M to allow observation of fluorescent emission. The LC cells used in the experiment consisted of LC sandwiched between two square glass plates, each with a thickness of 0.75 mm and dimensions of $2\times2\,\mathrm{cm}^2$, coated with a thin layer of indium tin oxide (ITO). A 20 nm layer of polyimide SUNEVER 5291 (Nissan) was coated on top of the ITO layer and then rubbed with a velvet cloth along one edge to ensure planar alignment of the LC molecules at the surfaces in that direction. The two glass plates were glued together so that the rubbing directions of both glasses were in anti-parallel orientation. The thickness of the gap between the plates was defined with spacers mixed into the UV glue used to bond the glass plates. The diameters of the spacers used were 4 µm and 9 µm. To ensure sufficient focusing of the laser light into the LC cell from the side, two edges of the upper and lower glass plates, parallel to the rubbing direction, were completely aligned, while the other two edges were slightly separated to provide space for filling the LC cell. Additionally, the gap on the aligned sides was sealed with a thin layer of UV-

curable glue (NOA 68, Norland Products, refractive index 1.54) before the LC cell was filled with LC. The LC was injected into the cell in the isotropic phase at 40 °C by capillary forces and then cooled to the nematic phase at room temperature. We optically checked the alignment of the LC near the glued edge, and the glue provided good planar anchoring, so the alignment remained consistent near the edge. To reorient the LC molecules from planar to homeotropic orientation, we applied an alternating electric field to the conductive ITO layers between the glass plates with an amplitude of 20 V (corresponding to an electric field $E_{\mathrm{AC}} = 2\,\mathrm{V\,\mu m^{-1}}$) and a frequency of 5 kHz. The same cells remained functional and produced reproducible structures over months of repeated use, as the nematic–isotropic transition is fully reversible and causes no material degradation.

Optical setup

The setup for studying in-plane beam control consisted of two main parts: optical tweezers to heat the LC layer and a setup to focus the beam into the LC layer from the side. It was built around an inverted optical microscope (Nikon Eclipse TE2000-E) equipped with a 10×, 0.30NA objective, which was used to observe the LC cell and to focus IR control beam into the LC cell. The source of laser light used for heating the ITO layer was optical tweezers (Aresis Tweez 200si) with a CW infrared laser beam (1064 nm, 5 W). The optical output power of the IR beam is variable, and the highest power used in experiments was 200 mW. Optical tweezers enable the creation of complex patterns of control beam foci positions in the observation plane by using acousto-optic deflection (AOD) of the laser beam. The beam position is switched between predefined points with a switching rate of 100 kHz and also the strength of the beam in each position can be controlled independently. A continuous-wave laser at 532 nm (CPS532, Thorlabs) with 4.5 mW power was used and coupled into the LC layer from the side. An aspheric lens (f =18.4 mm, 0.15NA) was used to focus the beam into the cell gap through the thin layer of the glue that closed the cell gap before entering the LC, which helped to maintain the set polarization of light also in the LC. The waist of the focused beam in the LC layer was $w_0 \approx 3{-}4\,\mu\mathrm{m}$ and the divergence was around 4° (0.1NA). The polarization and intensity of light were controlled using a rotatable polarizer and an attenuator. Typical power of the in-plane beam used was 0.23 mW. For the optical logic gates, lasers with wavelengths of 674 nm and 450 nm and power of 4.5 mW were used. We combined them using a dichroic mirror and focused them into the LC cell through the same lens from the side.

To observe both the LC structures and optical beam trajectory within the LC layer, we used the same 10× objective as for the IR control beam. To observe the isotropic structures and changes in refractive index, a crossed polarizer and analyzer with the combination of an LED light source were used. The beam trajectory was captured by imaging the optical scattering of the laser beam or by imaging fluorescent light in cells with added fluorescent dye. We used two cameras with different fields of view (iDS UI-3280CP and Sony ILCE-7M4).

Modeling of liquid crystal structures

The melted regions (i.e., LC structures) were modeled here as two-dimensional domains using Signed Distance Functions (SDFs). The 2D cross-section is considered to be in the mid-plane along the thickness of the LC cell. Based on the SDF $f(\mathbf{r})$, the approximate director configuration $n(\mathbf{r})$ and temperature profile $T(\mathbf{r})$ were calculated. Based on $T(\mathbf{r})$, the temperature-dependent ordinary $n_{\mathrm{o}}(T)$ and extraordinary $n_{\mathrm{e}}(T)$ refractive indices were calculated. For more information, please see Supplementary Information.

Combining the director configuration and the temperature dependent n_{o} and n_{e} gives us

the final dielectric profile $\varepsilon(\mathbf{r})$ of the structure as:

$$\varepsilon_{ij}(\mathbf{r}) = (\varepsilon_{\parallel}(\mathbf{r}) - \varepsilon_{\perp}(\mathbf{r}))n_i(\mathbf{r})n_j(\mathbf{r}) + \delta_{ij}\varepsilon_{\perp}(\mathbf{r}), \tag{1}$$

where $\varepsilon_{\parallel}(\mathbf{r}) = n_e^2(\mathbf{r})$ and $\varepsilon_{\perp}(\mathbf{r}) = n_o^2(\mathbf{r})$.

We used two design approaches for the LC structures: direct SDF design via the SPOMSO package [53], and an inverse design combining topology and shape optimization. For all designs, the dielectric tensor field is derived from the SDFs and projected onto a rectangular grid to generate the arrays required for light propagation simulations.

Light propagation simulations

The light propagation simulations were either used to simulate the electromagnetic fields in the LC cell (steady-state simulations), the transmitted flux (transmission simulations) through an LC cell or the diffraction spectra (diffraction simulations).

Light propagation through LC structures was simulated using the FDTD method in Meep [54]. The 2D simulation volumes, defined on a square grid with a resolution of $36\,\mathrm{pts}\,\mu\mathrm{m}^{-1}$, were enclosed by a $2\,\mu\mathrm{m}$ thick Perfectly Matched Layer (PML). In transmission simulations, a monochromatic pulsed source emitted an E_y or E_z polarized Gaussian beam ($\lambda = 532\,\mathrm{nm}$, $64\,\mathrm{nm}$ bandwidth, $10\,\mu\mathrm{m}$ waist) along the x-axis. Flux recorded at monitors was normalized against an empty simulation volume, with simulations running until the relative flux difference dropped below 10^{-8}. Diffraction simulations extended this by using Meep's near-to-far field method to propagate recorded fields through free space. For steady-state simulations, the pulsed source was replaced by a continuous Gaussian beam of identical characteristics. Fields across the entire volume were exported once the simulation time reached twice the duration required for fields to traverse the volume, ensuring a steady state was achieved.

Optimization of liquid crystal structures

Inverse design was performed via density-based topology optimization on a square grid with a $10\,\mathrm{pts}\,\mu\mathrm{m}^{-1}$ resolution. In each iteration, a transmission simulation calculated the objective function (e.g., average intensity) and its gradient with respect to every optimization parameter. These gradients were passed to the optimizer to adjust the spatially dependent dielectric function, repeating until the objective function converged (relative difference $< 10^{-8}$) or reached a 500-step limit. By using E_z polarized sources and keeping the director in the xy plane, the problem was simplified to the optimization of the ε_{zz} component alone. The optimization framework was developed in Python using the Meep FDTD method [54] with its adjoint solver [40]. The Method of Moving Asymptotes (MMA) [55] from the NLopt package [56] served as the optimization algorithm, with gradients calculated via automatic differentiation using the JAX library [57]. For a detailed description of the topology optimization algorithm see Supplementary Information.

Unconstrained topology optimization often yields experimentally unrealizable features, such as structures smaller than $5\,\mu\mathrm{m}$ or temperature fields inconsistent with isotropic regions. To address this, we developed custom mapping functions to enforce manufacturing constraints (see Supplementary Information).

To minimize the number of control beams needed to produce a structure that satisfies the optimization criteria we used shape optimization. The goal was to optimize the positions of control beams that produce isotropic disks with fixed radii and best match the structure obtained by topology optimization. Optimization concluded upon reaching a relative difference in cost function below 10^{-12} (within 1200 iterations), after which the final $\varepsilon_{zz}(\mathbf{r})$ was calculated.

To further refine the dielectric structure, these disk positions served as initial conditions for a second shape optimization phase incorporating FDTD simulations. This stage followed the same algorithmic structure as the topology optimization, but optimized the positions of the isotropic zones directly. In each iteration, a mapping function converted these coordinates into a dielectric profile, rather than applying constraints to the structure itself.

Overall, our inverse design approach includes three optimization stages: first, the topology optimization; second, the temperature profile matching shape optimization; and finally, the photonics shape optimization, yielding optimized and targeted structures that are also compliant with the experimental manufacturing and material constraints. As a representative example, the full inverse design of the beam splitter in Fig. 3e completes within two days on a single multi-core machine. The second step contributes only a few minutes and is negligible in comparison. The overall optimization time depends on the simulation-volume size and resolution, the number of parameters, and the complexity of the objective including the manufacturing constraints. For more details regarding the algorithm, see the Supplementary Information.

Acknowledgments

The authors thank Janja Milivojević for assembling LC cells. This project has received funding from the Slovenian Research and Innovation Agency (ARIS) (P1-0099, P1-0192, N1-0336 and J1-5000). This work is supported by ERC grant (SoftQuanta, 101170123). Funded by the European Union. Views and opinions expressed are however those of the author(s) only and do not necessarily reflect those of the European Union or the European Research Council Executive Agency. Neither the European Union nor the granting authority can be held responsible for them.

Competing interest

The authors declare no competing interests.

Author contributions

M.H. conceived the original idea. Z.K. performed all the experimental work and analysis of the results. P.R. performed the theoretical work and simulations. M.H. and M.R. supervised the study. All authors wrote the manuscript and approved the final version of the paper.

Data availability

The data that support the findings of this article are openly available on Zenodo (DOI: 10.5281/zenodo.19127865). The code for data analysis and simulations is available from the corresponding authors upon reasonable request.

References

[1] Iam-Choon Khoo. *Liquid crystals*. John Wiley & Sons, 2022.

[2] Jeroen Beeckman, Kristiaan Neyts, and Pieter J. M. Vanbrabant. Liquid-crystal photonic applications. *Optical Engineering*, 50(8):081202, 2011.

[3] Dimitrios C. Zografopoulos, Rita Asquini, Evangelos E. Kriezis, Antonello d'Alessandro, and Romeo Beccherelli. Guided-wave liquid-crystal photonics. *Lab on a Chip*, 12(19):3598–3610, 2012.

[4] Ting Wei, Peng Chen, Ming-Jie Tang, Guang-Xing Wu, Zhao-Xian Chen, Zhi-Xiong Shen, Shi-Jun Ge, Fei Xu, Wei Hu, and Yan-Qing Lu. Liquid-Crystal-Mediated Active Waveguides toward Programmable Integrated Optics. *Advanced Optical Materials*, 8(10):1902033, 2020.

[5] J. Sun, A. K. Srivastava, L. Wang, V. G. Chigrinov, and H. S. Kwok. Optically tunable and rewritable diffraction grating with photoaligned liquid crystals. *Optics Letters*, 38(13):2342, 2013.

[6] Junji Kobashi, Hiroyuki Yoshida, and Masanori Ozaki. Planar optics with patterned chiral liquid crystals. *Nature Photonics*, 10(6):389–392, 2016.

[7] Peter Ropač, Yu-Tung Hsiao, Brecht Berteloot, Yera Ussembayev, Inge Nys, Miha Ravnik, and Kristiaan Neyts. Liquid crystal 3d optical waveguides based on photoalignment. *Advanced Optical Materials*, 13(4):2402174, 2025.

[8] Inge Nys, Peter Ropač, Brecht Berteloot, Miha Ravnik, and Kristiaan Neyts. Highly dispersive liquid crystal diffraction gratings with continuously varying periodicity. *Journal of Molecular Liquids*, 383:122062, 2023.

[9] Urban Mur, Miha Ravnik, and David Seč. Controllable shifting, steering, and expanding of light beam based on multi-layer liquid-crystal cells. *Scientific Reports*, 12(1):352, 2022.

[10] Jeroen Beeckman, Kristiaan Neyts, and Marc Haelterman. Patterned electrode steering of nematicons. *Journal of Optics A: Pure and Applied Optics*, 8(2):214–220, 2006.

[11] Armando Piccardi, Alessandro Alberucci, Raouf Barboza, Oleksandr Buchnev, Malgosia Kaczmarek, and Gaetano Assanto. In-plane steering of nematicon waveguides across an electrically tuned interface. *Appl. Phys. Lett.*, 100(25):251107, 2012.

[12] Chan-Hee Han, Sang-Hee Lee, Sunghyun Bae, Jae Won Lee, and Seung-Won Oh. Advances in diffractive liquid crystal grating devices using patterned electrodes. *J. Inf. Disp.*, 25(4):367–377, 2024.

[13] A Piccardi, G Assanto, Liana Lucchetti, and Francesco Simoni. All-optical steering of soliton waveguides in dye-doped liquid crystals. *Applied Physics Letters*, 93(17), 2008.

[14] Marco Peccianti and Gaetano Assanto. Nematicons. *Phys. Rep.*, 516(4):147–208, 2012.

[15] Gaetano Assanto. Nematicons: reorientational solitons from optics to photonics. *Liq. Cryst. Rev.*, 6(2):170–194, 2018.

[16] Guilhem Poy, Andrew J. Hess, Ivan I. Smalyukh, and Slobodan Žumer. Chirality-enhanced periodic self-focusing of light in soft birefringent media. *Phys. Rev. Lett.*, 125(7):077801, 2020.

[17] Cuiling Meng, Jin-Sheng Wu, and Ivan I. Smalyukh. Topological steering of light by nematic vortices and analogy to cosmic strings. *Nat. Mater.*, 22(1):64–72, 2023.

[18] Andrew J Hess, Guilhem Poy, Jung-Shen B Tai, Slobodan Žumer, and Ivan I Smalyukh. Control of light by topological solitons in soft chiral birefringent media. *Physical Review X*, 10(3):031042, 2020.

[19] Xiao Yu, Shan-Shan Chang, Zi-Ye Wang, Jiao Liu, Xing-Zhou Tang, Jin-Hui Chen, Bing-Xiang Li, and Yan-Qing Lu. Dynamic transition from branched flow of light to beam steering in disordered nematic liquid crystal. *Laser & Photonics Reviews*, 18(10):2400366, 2024.

[20] Xiao Yu, Xin-Yu Fang, Jing-Qi Tian, Xing-Zhou Tang, Zi-Ye Wang, Jin-Hui Chen, Yan-Qing Lu, and Bing-Xiang Li. On-demand tailoring of optical branched flow via soft matter domain engineering. *Laser & Photonics Reviews*, 19(15):2401717, 2025.

[21] Wim Bogaerts, Daniel Pérez, José Capmany, David A. B. Miller, Joyce Poon, Dirk Englund, Francesco Morichetti, and Andrea Melloni. Programmable photonic circuits. *Nature*, 586(7828):207–216, 2020.

[22] Matthias Wuttig, Harish Bhaskaran, and Thomas Taubner. Phase-change materials for non-volatile photonic applications. *Nat. Photonics*, 11(8):465–476, 2017.

[23] Carlos Errando-Herranz, Alain Yuji Takabayashi, Pierre Edinger, Hamed Sattari, Kristinn B. Gylfason, and Niels Quack. MEMS for photonic integrated circuits. *IEEE J. Sel. Top. Quantum Electron.*, 26(2):1–16, 2020.

[24] Cameron L. C. Smith, Uwe Bog, Snjezana Tomljenovic-Hanic, Michael W. Lee, Darran K. C. Wu, Liam O'Faolain, Christelle Monat, Christian Grillet, Thomas F. Krauss, Christian Karnutsch, Ross C. McPhedran, and Benjamin J. Eggleton. Reconfigurable microfluidic photonic crystal slab cavities. *Opt. Express*, 16(20):15887–15896, 2008.

[25] Christian Grillet, Christelle Monat, Cameron L. Smith, Michael W. Lee, Snjezana Tomljenovic-Hanic, Christian Karnutsch, and Benjamin J. Eggleton. Reconfigurable photonic crystal circuits. *Laser Photonics Rev.*, 4(2):192–204, 2010.

[26] Tatsuhiro Onodera, Martin M Stein, Benjamin A Ash, Mandar M Sohoni, Melissa Bosch, Ryotatsu Yanagimoto, Marc Jankowski, Timothy P McKenna, Tianyu Wang, Gennady Shvets, et al. Arbitrary control over multimode wave propagation for machine learning. *Nature Physics*, 22(1):164–171, 2025.

[27] Ryotatsu Yanagimoto, Benjamin A Ash, Mandar M Sohoni, Martin M Stein, Yiqi Zhao, Federico Presutti, Marc Jankowski, Logan G Wright, Tatsuhiro Onodera, and Peter L McMahon. Programmable on-chip nonlinear photonics. *Nature*, 649:330–337, 2025.

[28] Ole Sigmund and Kurt Maute. Topology optimization approaches. *Struct. Multidiscip. Optim.*, 48:1031–1055, 2013.

[29] H. Men, K. Y. K. Lee, R. M. Freund, J. Peraire, and S. G. Johnson. Robust topology optimization of three-dimensional photonic-crystal band-gap structures. *Opt. Express*, 22(19):22632–22648, 2014.

[30] Fengwen Wang, Jakob S. Jensen, and Ole Sigmund. High-performance slow light photonic crystal waveguides with topology optimized or circular-hole based material layouts. *Photonics Nanostruct. Fundam. Appl.*, 10(4):378–388, 2012.

[31] Jakob S. Jensen and Ole Sigmund. Systematic design of photonic crystal structures using topology optimization: Low-loss waveguide bends. *Appl. Phys. Lett.*, 84(12):2022–2024, 2004.

[32] Y. Elesin, B.S. Lazarov, J.S. Jensen, and O. Sigmund. Time domain topology optimization of 3D nanophotonic devices. *Photonics Nanostruct. Fundam. Appl.*, 12(1):23–33, 2014.

[33] Louise F. Frellsen, Yunhong Ding, Ole Sigmund, and Lars H. Frandsen. Topology optimized mode multiplexing in silicon-on-insulator photonic wire waveguides. *Opt. Express*, 24(15):16866–16873, 2016.

[34] Alexander Y Piggott, Jesse Lu, Konstantinos G Lagoudakis, Jan Petykiewicz, Thomas M Babinec, and Jelena Vučković. Inverse design and demonstration of a compact and broadband on-chip wavelength demultiplexer. *Nat. Photonics*, 9:374–377, 2015.

[35] Rasmus E. Christiansen, Zin Lin, Charles Roques-Carmes, Yannick Salamin, Steven E. Kooi, John D. Joannopoulos, Marin Soljačić, and Steven G. Johnson. Fullwave Maxwell inverse design of axisymmetric, tunable, and multi-scale multi-wavelength metalenses. *Opt. Express*, 28(23):33854–33868, 2020.

[36] Evan W. Wang, David Sell, Thaibao Phan, and Jonathan A. Fan. Robust design of topology-optimized metasurfaces. *Opt. Mater. Express*, 9(2):469–482, 2019.

[37] Kiyoul Yang, Jinhie Skarda, Michele Cotrufo, Avik Dutt, Geun Ahn, Mahmoud Sawaby, Dries Vercruysse, Amin Arbabian, Shanhui Fan, Andrea Alù, and Jelena Vuckovic. Inverse-designed non-reciprocal pulse router for chip-based lidar. *Nat. Photonics*, 14:369–374, 2020.

[38] Lu He, Furong Zhang, Huizhen Zhang, Ling-Jun Kong, Weixuan Zhang, Xingsheng Xu, and Xiangdong Zhang. Topology-optimized ultracompact all-optical logic devices on silicon photonic platforms. *ACS Photonics*, 9:597–604, 2022.

[39] Alec M. Hammond, Ardavan Oskooi, Steven G. Johnson, and Stephen E. Ralph. Photonic topology optimization with semiconductor-foundry design-rule constraints. *Opt. Express*, 29(15):23916–23938, 2021.

[40] Alec M. Hammond, Ardavan Oskooi, Mo Chen, Zin Lin, Steven G. Johnson, and Stephen E. Ralph. High-performance hybrid time/frequency-domain topology optimization for large-scale photonics inverse design. *Opt. Express*, 30(3):4467–4491, 2022.

[41] Shin-Tson Wu and Khoon-Cheng Lim. Absorption and scattering measurements of nematic liquid crystals. *Applied optics*, 26(9):1722–1727, 1987.

[42] Laura Cattaneo, Matteo Savoini, Igor Muševič, Alexey Kimel, and Theo Rasing. Ultrafast all-optical response of a nematic liquid crystal. *Optics express*, 23(11):14010–14017, 2015.

[43] K.W. Busch and M.A. Busch. *Multielement Detection Systems for Spectrochemical Analysis*, chapter 6.6.5. Chemical Analysis: A Series of Monographs on Analytical Chemistry and Its Applications. Wiley, 1991.

[44] Anatoly Patsyk, Uri Sivan, Mordechai Segev, and Miguel A Bandres. Observation of branched flow of light. *Nature*, 583(7814):60–65, 2020.

[45] Shan-shan Chang, Ke-Hui Wu, Si-jia Liu, Zhi-Kang Lin, Jin-bing Wu, Shi-jun Ge, Lu-Jian Chen, Peng Chen, Wei Hu, Yadong Xu, et al. Electrical tuning of branched flow of light. *Nature Communications*, 15(1):197, 2024.

[46] Jaroslaw Mysliwiec, Alina Szukalska, Adam Szukalski, and Lech Sznitko. Liquid crystal lasers: the last decade and the future. *Nanophotonics*, 10(9):2309–2346, 2021.

[47] Harry Coles and Stephen Morris. Liquid-crystal lasers. *Nature Photonics*, 4(10):676–685, 2010.

[48] SeongYong Cho, Hiroyuki Yoshida, and Masanori Ozaki. Emission direction-tunable liquid crystal laser. *Advanced Optical Materials*, 8(16):2000375, 2020.

[49] David J. Brady and Demetri Psaltis. Holographic interconnections in photorefractive waveguides. *Appl. Opt.*, 30(17):2324–2333, 1991.

[50] Vitaliy Sultanov, Aljaž Kavčič, Emmanouil Kokkinakis, Nerea Sebastián, Maria V Chekhova, and Matjaž Humar. Tunable entangled photon-pair generation in a liquid crystal. *Nature*, 631(8020):294–299, 2024.

[51] Sara Klopčič, Aljaž Kavčič, Nerea Sebastián, and Matjaž Humar. Electrically and geometrically tunable photon pair entanglement from ferroelectric nematic liquid crystal. *Advanced Science*, 13(3):e15206, 2026.

[52] Jun Li, Sebastian Gauza, and Shin-Tson Wu. Temperature effect on liquid crystal refractive indices. *J. Appl. Phys.*, 96(1):19–24, 2004.

[53] Peter Ropač. Aegolius: SPOMSO – Signed Distance Function Python package, 2024. Accessed: 2025-06-14.

[54] Ardavan F. Oskooi, David Roundy, Mihai Ibanescu, Peter Bermel, J.D. Joannopoulos, and Steven G. Johnson. Meep: A flexible free-software package for electromagnetic simulations by the fdtd method. *Comput. Phys. Commun.*, 181(3):687–702, 2010.

[55] Krister Svanberg. A class of globally convergent optimization methods based on conservative convex separable approximations. *SIAM J. Optim.*, 12(2):555–573, 2002.

[56] Steven G. Johnson. The NLopt nonlinear-optimization package. online, 2007.

[57] James Bradbury, Roy Frostig, Peter Hawkins, Matthew James Johnson, Chris Leary, Dougal Maclaurin, George Necula, Adam Paszke, Jake VanderPlas, Skye Wanderman-Milne, and Qiao Zhang. JAX: composable transformations of Python+NumPy programs, 2018.

[58] Boyan S Lazarov, Fengwen Wang, and Ole Sigmund. Length scale and manufacturability in density-based topology optimization. *Arch. Appl. Mech.*, 86:189–218, 2016.

[59] Iñigo (iq) Quilez. Articles and tutorials on computer graphics and shaders. Online, 2025. https://iquilezles.org/articles/, accessed 14 June 2025.

[60] Diederik P. Kingma and Jimmy Ba. Adam: A method for stochastic optimization, 2017. arXiv:1412.6980 [cs.LG].

[61] DeepMind, Igor Babuschkin, Kate Baumli, Alison Bell, Surya Bhupatiraju, Jake Bruce, Peter Buchlovsky, David Budden, Trevor Cai, Aidan Clark, Ivo Danihelka, Antoine Dedieu, Claudio Fantacci, Jonathan Godwin, Chris Jones, Ross Hemsley, Tom Hennigan, Matteo Hessel, Shaobo Hou, Steven Kapturowski, Thomas Keck, Iurii Kemaev, Michael King, Markus Kunesch, Lena Martens, Hamza Merzic, Vladimir Mikulik, Tamara Norman, George Papamakarios, John Quan, Roman Ring, Francisco Ruiz, Alvaro Sanchez, Laurent Sartran, Rosalia Schneider, Eren Sezener, Stephen Spencer, Srivatsan Srinivasan, Miloš Stanojević, Wojciech Stokowiec, Luyu Wang, Guangyao Zhou, and Fabio Viola. The DeepMind JAX Ecosystem, 2020. http://github.com/google-deepmind.

[62] Robert Bridson. Fast poisson disk sampling in arbitrary dimensions. In *ACM SIGGRAPH 2007 Sketches*, SIGGRAPH '07, page 22–es, New York, NY, USA, 2007. Association for Computing Machinery.